Simulations of the NASA Langley 14- by 22-Foot Subsonic Tunnel for the Juncture Flow Experiment

Henry C. Lee
Science and Technology Corporation
Moffett Field, CA 94035
USA

henry.c.lee@nasa.gov

Thomas H. Pulliam
NASA Ames Research Center
Moffett Field, CA 94035
USA

thomas.h.pulliam@nasa.gov

Chris L. Rumsey, Jan-Renee Carlson
NASA Langley Research Center
Hampton, VA 23681
USA

c.l.rumsey@nasa.gov, jan-renee.carlson@nasa.gov

ABSTRACT

NASA's Transformational Tools and Technologies Program's Juncture Flow experiment aims to provide data to improve Computational Fluid Dynamics (CFD) modeling in the juncture flow region. The experiment is planned to provide validation-quality data for CFD that focuses on the separation bubble near the wing-body juncture trailing edge region. Because wind tunnel tests associated with the Juncture Flow project have been designed for the purpose of CFD validation, considerable effort is going into modeling and simulating the wind tunnel. This is not only important because wind tunnel wall effects can play a role in integrated testing uncertainties, but also because the better the boundary conditions are known, the better CFD can accurately represent the experiment. This paper builds on the recent CFD efforts[1] to model the NASA Langley 14- by 22-Foot Subsonic Tunnel. Current best practices in simulating wind tunnels are evaluated. The features of each method, as well as some of their pros and cons, are highlighted. Boundary conditions and modeling techniques currently used by CFD for empty-tunnel simulations are also described. Preliminary CFD studies associated with modeling the Juncture Flow model are summarized, with the intention to determine sensitivities of the flow near the wing-body juncture region of the model to a variety of modeling decisions.

1.0 INTRODUCTION

The NASA Juncture Flow (JF) experiment[2,3] conducted in late 2017 and early 2018 in the NASA Langley 14- by 22-Foot Subsonic Tunnel (14x22), is designed to measure CFD-validation-quality data for the onset and

progression of a trailing edge separation near the wing-body juncture of an aircraft-like configuration. These particular flow features are considered difficult for state-of-the-art CFD methods to reliably predict.[4] The experiment will provide a significant amount of detailed information to help enable improvement in the methods.

In the 2017-2018 experimental campaign, laser Doppler velocimetry (LDV) and particle image velocimetry (PIV) were used to document the flow field upstream and within the corner separation region. The LDV system was carried inside the model's fuselage, and its lasers passed pass through windows installed on the side of the model near several regions of interest. These regions include the wing trailing edge area (where the separation occurs), as well as the wing leading edge area, and an area well upstream on the fuselage nose. The latter two areas will help to establish oncoming boundary conditions for use in CFD validation studies.

With JF testing taking place in the 14x22, considerable effort is being expended to understand CFD's ability to model the tunnel's flow characteristics. Boundary conditions are considered important inputs for CFD validation, and may influence integrated testing uncertainties.[5] The importance of this type of wind tunnel documentation has been cited in the literature.[5,6] Making these types of measurements is a challenging task so CFD will likely be needed for detailed assessment.

When comparing against experimental data from wind tunnels, many CFD studies routinely include the wind tunnel walls as part of the computational model. There is always uncertainty arising from attempting to "correct" wind tunnel data to freestream conditions, and direct one-to-one comparison is more straightforward when all geometry is included. Typically, the tunnel walls are modeled as solid viscous surfaces. Often, the extent of accurate physical modeling, for example using viscous tunnel walls, is traded for a reduction in computational resources (time and/or computer memory demands) by modeling the parts of the tunnel walls as inviscid surfaces.

Early CFD work for this wind tunnel was performed by Nayani et al. [6,7]. In Nayani et al. [6] only the high-speed leg of the tunnel was modeled. When running CFD, the as-built wind-tunnel shape (measured with laser scanning) yielded upflow angles closer to those measured in the tunnel than the as-designed shape results. Wall pressures and boundary layer profiles were in reasonable agreement with experimental data. In Nayani et al. [7] the entire circuit was modeled. In the current study, we do not repeat the entire circuit effort, but rather focus on simulation of the high-speed leg only. We only include the as-built shape, since Nayani et al. [6,7] already demonstrated its importance. Figure 1-1 shows the full circuit of the 14x22 wind tunnel, with the high speed leg outlined. Figure 1-2 describes the sections of the high speed leg of the 14x22.

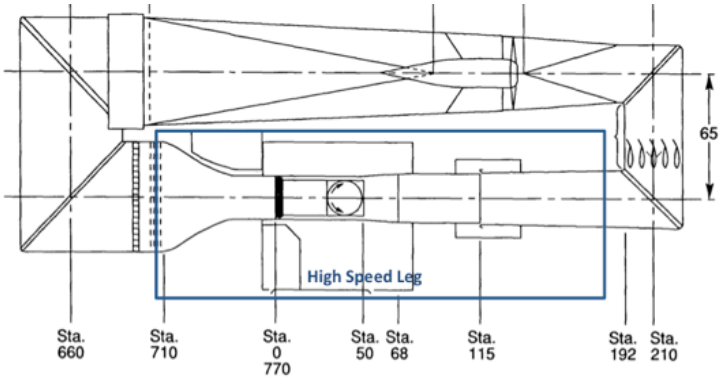

Figure 1-1: 14x22 high speed leg highlighted

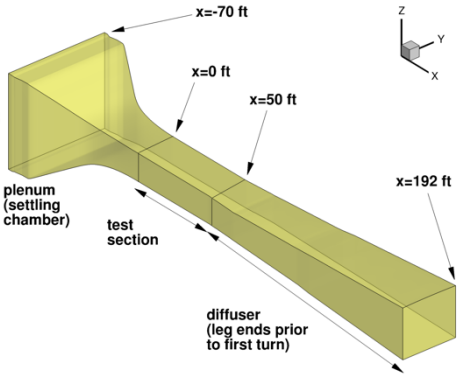

Figure 1-2: Dimensions of 14x22

Figure 1: 14- by 22-Foot Subsonic Tunnel, High Speed Leg

More recently, Rumsey et al. [1] explored multiple CFD methods in simulating the 14x22 tunnel at the JF experimental conditions. This paper expands on the prior work performed.

2.0 COMPUTATIONAL FLUID DYNAMICS (CFD) SETUP

This section describes the CFD simulation setup. A brief introduction to the CFD code and numerical schemes used will be presented, followed by a variety of simulations of the empty 14x22 with a focus on the boundary conditions and modeling techniques.

2.1 OVERFLOW CFD Solver

OVERFLOW 2.2n is a three-dimensional time-marching implicit Navier-Stokes structured overset code that is nominally second-order spatially accurate. The flux-difference splitting third-order Roe scheme[8] is used for the convective fluxes, and all other terms are differenced to second-order accuracy. Various inviscid flux and implicit algorithms are available, as well as multiple turbulence models. OVERFLOW requires that all overset grids be assembled and processed using Pegasus[9] or DCF[10] for domain connectivity. More information can be found at the OVERFLOW website.[11]

The OVERFLOW cases were run with the Roe upwind scheme and the ARC3D diagonalized Beam-Warming scalar pentadiagonal scheme.[8,11] Full multigrid cycles were used to help initialize the solution and help accelerate the convergence. Solutions were run in the steady-state mode. The Spalart-Allmaras turbulence model[12] with the rotation-curvature (RC) correction[13] and quadratic constitutive relation (QCR)[14] (SA-RC-QCR2000) were used.

2.2 CFD Empty Tunnel Modeling

There are a variety of modeling choices that can be made when modeling the wind tunnel, all of which could affect the flowfield, solution convergence, simulation cost, etc. A few tunnel modeling options were explored in Rumsey et al. [1], and a select few cases from that reference will be presented again in this paper. Ultimately, we would like to estimate the sensitivity of wind tunnel data of interest in the wind tunnel. Such estimates would help to establish error bounds on the measured data. This is difficult to achieve in experiments, but may be possible to assess to some degree via CFD simulations.

2.3 Boundary Conditions

For internal flows, the total pressure and total temperature are typically specified at the inflow boundary.[15,16] This boundary condition uses information from forward-traveling waves (Riemann invariants) that are interpolated from the interior of the computational domain. Additional information used to define the boundary state is the incoming flow angle. Setting the static pressure is the most often used outflow boundary condition. Additional details on these boundary conditions can be found in Refs [15,16].

While the boundary conditions for an inviscid flow simulation can be exactly determined, viscous flow simulations are subject to viscous losses. For viscous flow simulations, the static pressure at the outflow boundary (also called the back pressure) will be slightly lower than the inviscid value. The degree of viscous loss is not known a priori; therefore, the back pressure is iterated to attain the desired Mach number in the test section. Despite the static pressure being a numerically consistent outflow boundary condition, it is highly reflective and can create transient pressure waves at solution startup that are often difficult for codes to recover from numerically. Alternative outflow boundary conditions exist,[15,16,17,18] but were not used in this study. Additionally, the static pressure boundary condition in the presence of reverse flow, can become quite unstable numerically leading to unphysical flow solutions occurring at the boundary.[19]

The tunnel conditions and boundary conditions used for the viscous simulations in this paper are listed in Table 1. The back pressures used are listed later in Table 2.

Table 1. Flow Conditions and Boundary Conditions

Walls BC	Mach	Reynolds Number [1/ft.]	Temperature [°R]	Inflow Pressure P_t/P_∞	Inflow Temperature T_t/T_∞	Outflow Pressure P/P_∞
OVERFLOW Viscous	0.2	1.31×10^6	560.6	1.02828	1.008	See Table 2

2.4 Empty Tunnel Grids

The high-speed leg of the 14x22 consists of three components: (1) the upstream settling chamber, (2) the test section, and (3) the downstream diffuser. A fourth component was added in this study, (4) the downstream diffuser extension, to mitigate the impact of corner flow separation in the diffuser on the outflow boundary. The various empty tunnel concepts explored in this study are listed in Table 2. The baseline configuration consists of just the high-speed leg of the 14x22, as shown in Figure 1-2. The upstream end (just aft of the screens in the tunnel) is located approximately 70 ft. upstream of the start of the test section that starts at x = 0 ft. The test section is 50 ft. long and is followed by a diffuser extending downstream. The diffuser is terminated at approximately x = 192 ft., just prior to the first turn of the physical tunnel geometry. A second topology, called extended diffuser, starts from the baseline grid and adds a 100 ft. long constant area downstream section starting from x = 192 ft.

To model the 14x22 tunnel systems in OVERFLOW, a series of overset grids were built.[20] A coarse, medium, and fine grid based on the baseline system were built, and a grid refinement study was performed. Twelve zones modeled the high-speed leg of the 14x22. The tunnel was split into four sections streamwise: plenum, test section, diffuser part 1, diffuser part 2. Each section was comprised of two viscous wall grids, and one core grid. The average grid spacing was varied to produce 3 levels of grid refinement: coarse (0.83 ft.), medium (0.5 ft.), and fine (0.25 ft.). The test section spacing for all three grids had a maximum spacing of 0.5 ft. Minimum spacing at the walls of the test section was less than 0.00001 ft. on all grids. The diffuser grids gradually coarsened downstream, with the expectation that the larger spacing would artificially dampen any reflections from the exit boundary condition. A maximum stretching ratio of 1.2 was used. The fourth and fifth OVERFLOW grid system is based on the extended diffuser topology. The diffuser here is extended 100 ft. streamwise, and the extended diffuser walls use an inviscid boundary condition. The last OVERFLOW grid system includes an inviscid inlet. The straight portion of the settling chamber from the inflow BC face to the start of the contraction was run inviscid.

Table 2. Empty Tunnel Grid Descriptions

Name	Wall BC	# Grid Points	Outflow Pressure P/P_∞	Notes
Baseline	Viscous	9,281,003	1.0190	Coarse
	Viscous	41,637,971	1.02119	Medium
	Viscous	118,687,475	1.02119	Fine
Inviscid Extended Diffuser[3]	Both	39,049,834	1.02188	Inviscid Extension
Inviscid Inlet & Extended Diffuser[3]	Both	39,049,834	1.02188	Inviscid Inlet+Extension

2.5 Tunnel Modeling Techniques

2.5.1 Tunnel Modeling

The various attempts at modeling and calculating the flow in the empty high-speed leg of the 14x22 are discussed in the following sections. Geometric variations and boundary condition variations will be discussed, as well as the effect of adding a diffuser extension.

The diffuser extension was proposed to help diffuse any subsonic characteristic waves from propagating upstream from the exit boundary condition, and to suppress corner separation or reverse flow occurring in the diffuser. The diffuser extension is coarsened as it extends downstream. Additionally, the extended diffuser can be run with inviscid walls. Boundary conditions utilized at the inlet and exit of (most) wind tunnel simulations are formulated often with inviscid assumptions, and having an inviscid wall at the exit may help the solution convergence. However, additional losses in the tunnel circuit were unintentionally incurred due to the additional boundary layer growth on the walls of the diffuser extension. The consequence, as will be seen later in this paper, is a lower test section Mach number, given the same boundary condition settings. In this sense, the baseline model and the extended diffuser model are two slightly different simulations.

In retrospect, a few other variations on geometry and boundary conditions should be considered, but will not be analyzed in this particular study. One variation that is often considered is constructing a constant area, upstream viscous plenum. The increase in local flow Mach number would help the solution convergence, reduce total grid count, and retain some boundary layer effects entering the test section.

2.5.2 Tunnel Speed Calculations

From the 14x22 calibration report by Gentry et al. [21], the tunnel is calibrated utilizing a series of probes at a tunnel station at 17.75 ft. For a first method, the simulated wind tunnel speed will be determined by probing the CFD solution at x = 17.75 ft. (along the centerline of the tunnel). This location is often where the center of the model is placed. This poses a problem for CFD, as the probe location will be blocked by the model.

A second method, based off of the 14x22 calibration report,[21] relies on calculating the tunnel speed from a static and total pressure probe. The stagnation pressure probe is near the front of the contraction inlet, and the static probe is just upstream of the test section. These pressure values are fed into a series of piecewise linear equations, calibrated to determine the velocity in the 14x22. A comparison of these two methods will be presented below in section 3.1.

To obtain the tunnel speed for either method, the exit pressure ratio is often iterated until the desired speeds are achieved in the test section. Small incremental changes to the back pressure are made until the tunnel speed matches the desired conditions. Often times, this process is manual and requires a lot of computational and human effort.

3.0 EMPTY TUNNEL SIMULATION RESULTS

3.1 OVERFLOW Grid Refinement Study

OVERFLOW viscous solutions using the baseline tunnel model with different grid resolutions are discussed in this section. The centerline Mach number and total pressure, shown in Figure 2, are nearly identical for the medium and fine grids, while the coarse grid shows a different result. This is most likely attributed to the large corner separation present in the coarse grid solution, as seen in Figure 3-1 that is not as pronounced in the finer grids. The drastic total pressure change at the exit for all the grid levels, seen in Figure 2-2, shows the need for OVERFLOW

to implement a similar blocking boundary condition that FUN3D utilized in Rumsey et al. [1]. Low Mach number preconditioning generally improves convergence behavior for these cases.

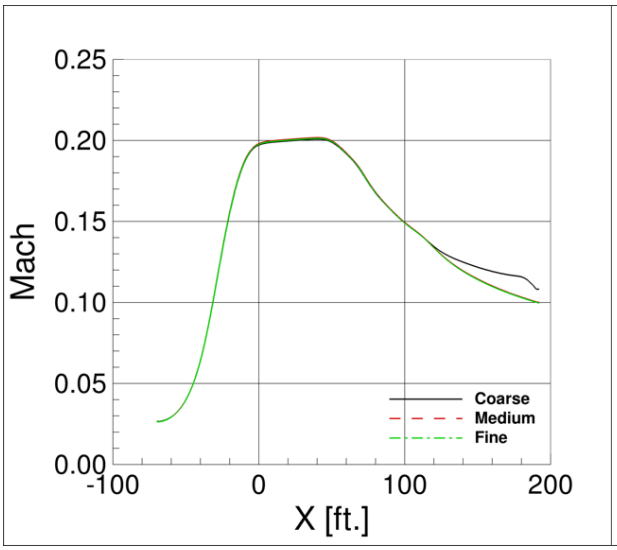

Figure 2-1: Centerline Mach number

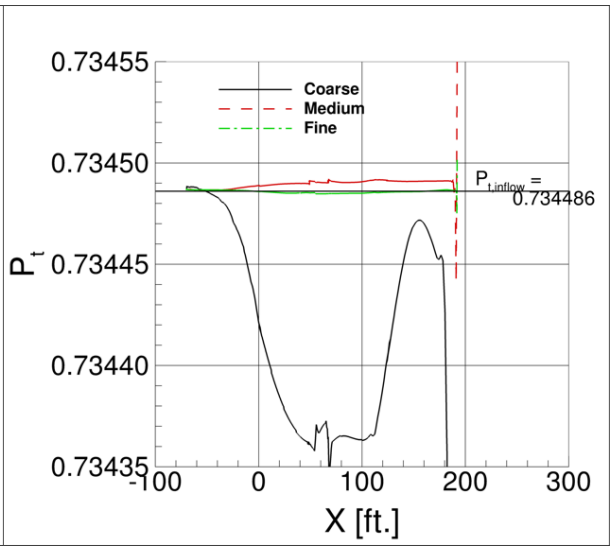

Figure 2-2: Centerline total pressure

Figure 2: Viscous walls, Grid Refinement Study

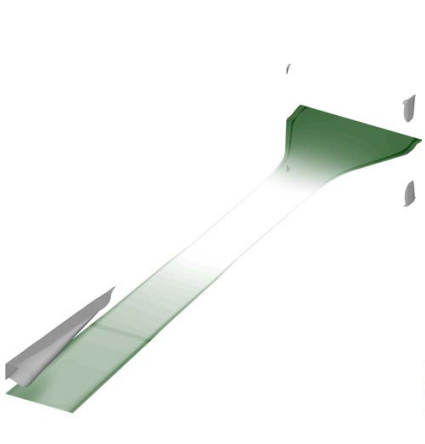

Figure 3-1: Coarse

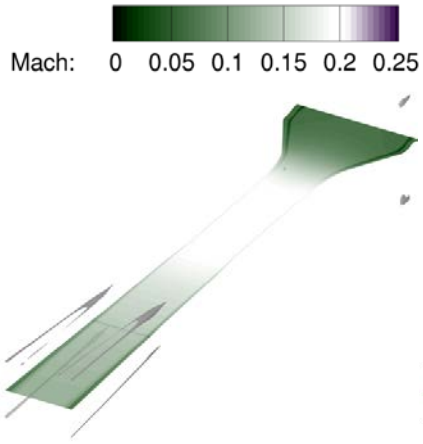

Figure 3-2: Medium

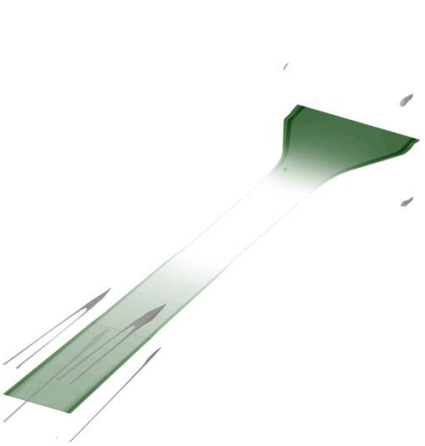

Figure 3-3: Fine

Figure 3: Z=0 Slice showing Mach contours and gray isosurfaces representing reverse flow, Grid Refinement Study

Tunnel Mach number for the grid refinement cases were calculated two ways: the wind tunnel method, which calculates the tunnel speed from the stagnation and static probe measurements, and direct query of the point (17.75, 0, 0) inside the test section, as described in Section 2.5.2. For the wind tunnel method, the stagnation pressure and static pressure were obtained from the sensor points. The pressure values were then fed into the same function used by the 14x22 to calculate the test section speed. This calculated tunnel Mach number is compared to the direct

probe at (17.75, 0, 0) in Table 3. The two different methods of calculating the Mach number produced values within one percent of each other. When a model is present in the tunnel, having a method for consistently and accurately duplicating the tunnel conditions in the CFD is important. The wind tunnel method is one way, but making other measurements for corroboration is also desirable. These other measurements might include isolated probes to measure velocity at specific locations away from the model, wall pressures, and diffuser pressures, for example.

Table 3: Calculated Mach number vs Direct Probe at (17.75,0,0)

Grid	Calculated Mach	Direct Mach Probe
Coarse	0.2023	0.1995
Medium	0.2029	0.2004
Fine	0.2025	0.2000

The residual history plots in Figure 4 show the residuals (lines represent the individual zones) for the three grid levels. The residuals all initially drop and then level out. By turning on the preconditioning, the residuals drop an additional 1 - 2 orders for the medium and fine grids. However, the large separation on the coarse grid prevents similar improvement on that grid. Note the peaks in the residual in Figure 4 correspond to a manual iterative change in the exit pressure ratio.

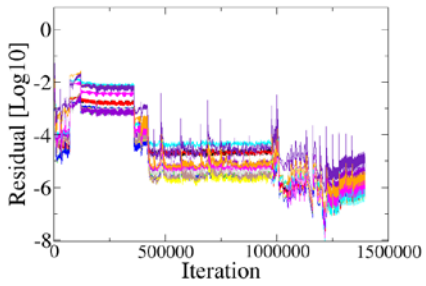

Figure 4-1: Coarse

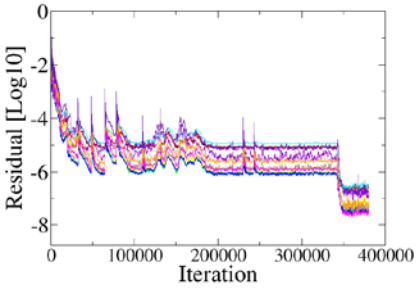

Figure 4-2: Medium

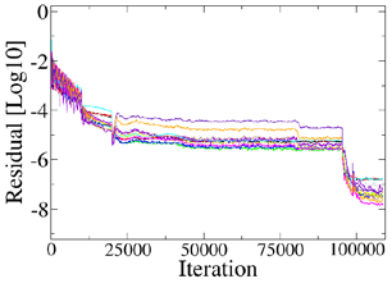

Figure 4-3: Fine

Figure 4: Solution Residuals, Grid Refinement Study

3.2 OVERFLOW Inviscid Inlet and Diffuser

The centerline Mach number and total pressure conservation are shown in Figure 5. The total pressure is better conserved by adding inviscid diffuser extension. The Mach numbers in the test section are nearly identical for all the cases shown. Figure 5-2 also shows a lower total pressure change at the exit boundary condition.

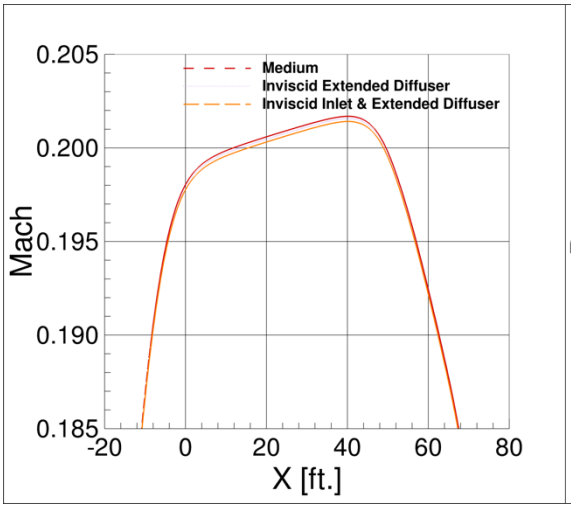

Figure 5-1: Centerline Mach number

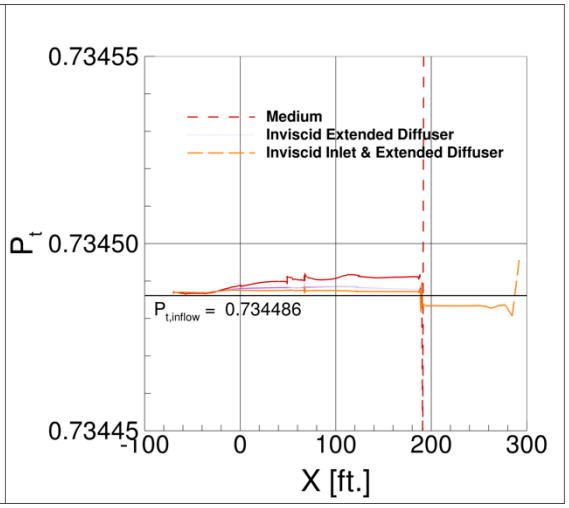

Figure 5-2: Centerline total pressure

Figure 5: Centerline values, Tunnel Modeling Study

There are subtle differences in running the inlet settling chamber (prior to the contraction) viscous vs. inviscid. The exit pressure ratios for both of the inviscid diffuser extension cases are identical, and Figure 6 shows that adding the inviscid inlet slightly increases the tunnel speed. There is also no corner separation in the inlet settling chamber as well, as seen in Figure 7. This makes sense, as there are no viscous losses over that short inlet portion, resulting in the slight speedup. The solution residual with the inviscid inlet, shown in Figure 8-2, shows that the solution is converging faster with less oscillations than the case without the inviscid inlet, seen in Figure 8-1. As before, each of the peaks corresponds to a manual change to the exit pressure ratio.

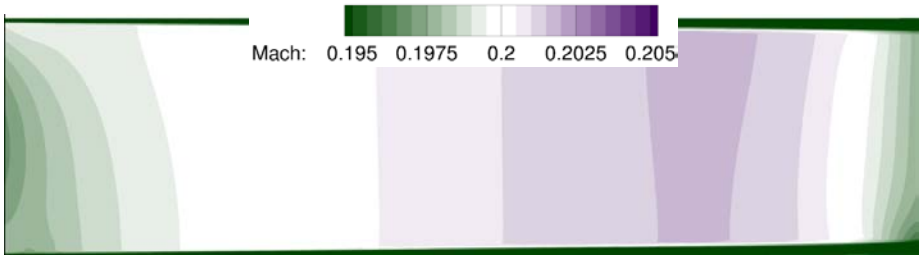

Figure 6-1: Inviscid Extended Diffuser

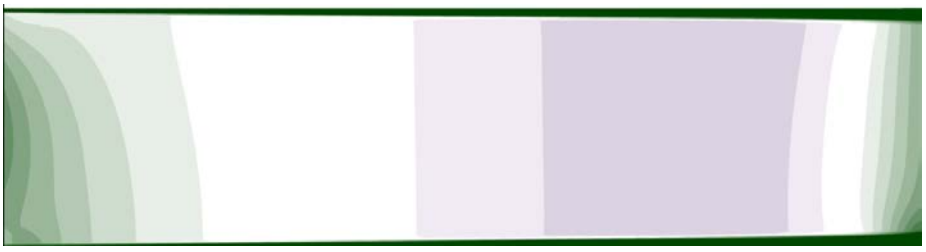

Figure 6-2: Inviscid Inlet + Inviscid Extended Diffuser

Figure 6: Y=0 Slice showing Mach contours, Tunnel Modeling Study

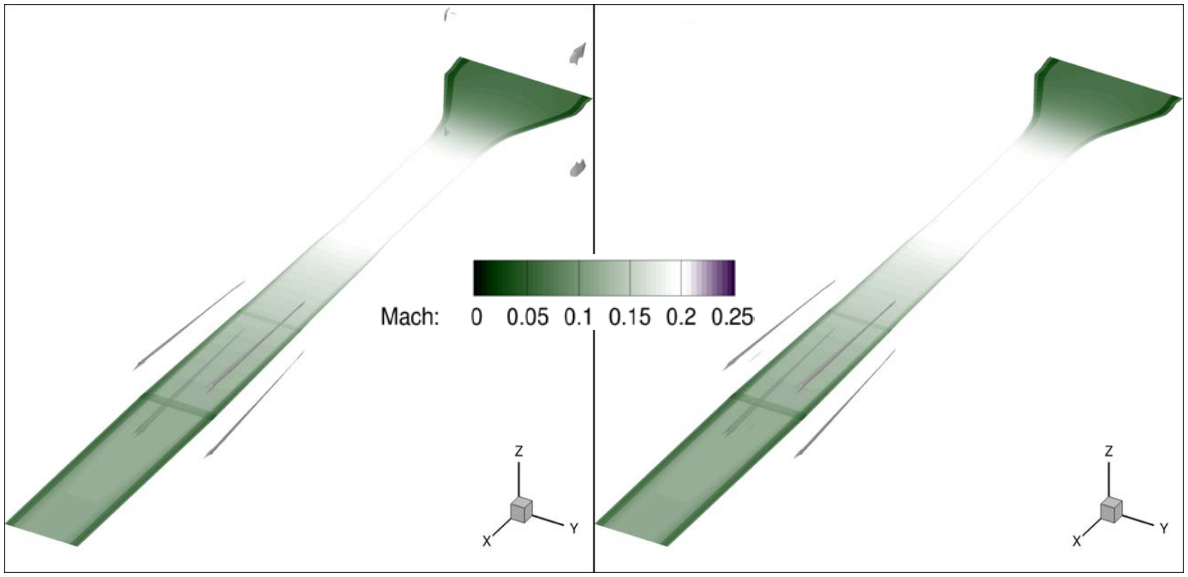

Figure 7-1: Inviscid Extended Diffuser **Figure 7-2: Inviscid Inlet + Inviscid Extended Diffuser**

Figure 7: Z=0 Slice showing Mach contours and gray isosurfaces representing reverse flow, Tunnel Modeling Study

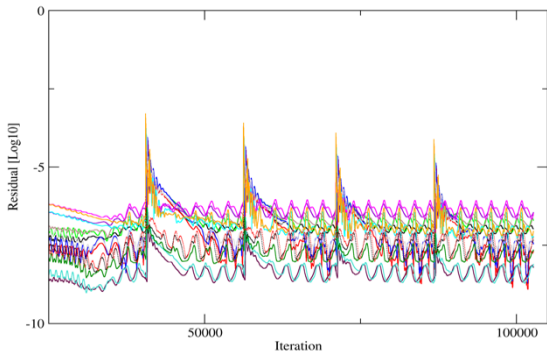

Figure 8-1: Inviscid Diffuser Extension

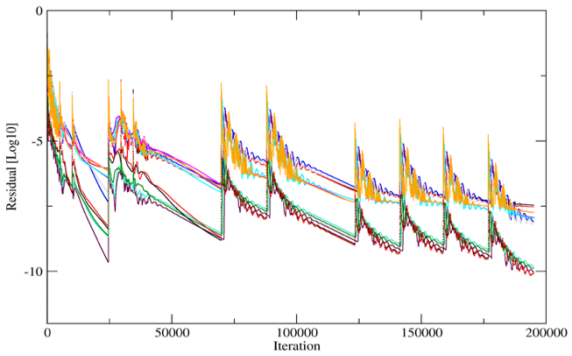

Figure 8-2: Inviscid Inlet + Inviscid Diffuser Extension

Figure 8: Solution Residuals, Tunnel Modeling Study

4.0 JUNCTURE FLOW SENSITVITY

4.1 Juncture Flow Model & Grids

In this section, we explore the influence of the support hardware on the Juncture Flow model (JFM). The JFM is configured with no leading edge horn installed on the starboard and port wings, and is at 8 percent scale based off of the Common Research Model.[4] The support hardware includes a roll sting and a mast. The mast is able to rotate and traverse up and down to place the JFM in the desired position in the tunnel. Figure 9 details the JFM with the support hardware. Figure 10 shows the JFM with all the support hardware as installed in the 14x22.

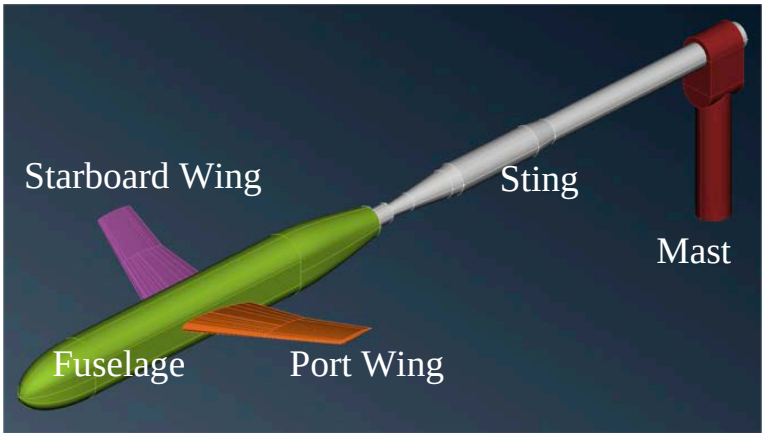

Figure 9: Juncture Flow Model 8% with Sting and Mast

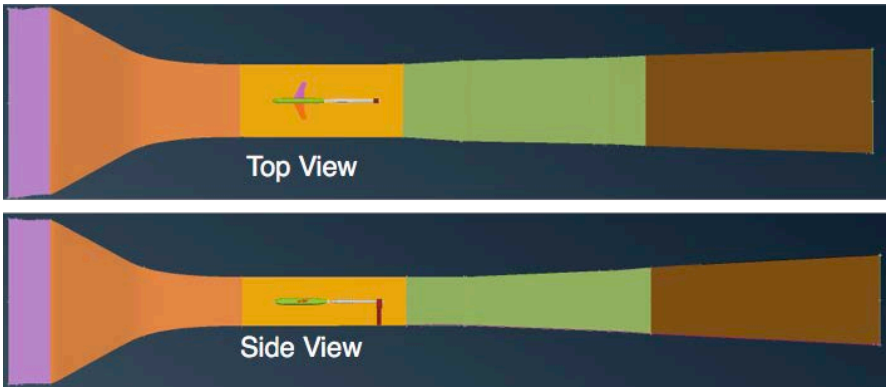

Figure 10: JFM 8% installed in the baseline 14x22, α = 0°

A series of overset grids were used to model the JFM. The grids were built using Chimera Grid Tools,[20] and domain connectivity was performed using DCF.[10] The JFM consists of a fuselage, and two wings. The fuselage is built from 3 zones, two of which span the length of the fuselage, and a nose cap grid. The wing grids share a common 6 zone topology: two collar grids covering the wing-fuselage junction, two grids spanning the wing, and two wing tip cap grids. Each pair of grids have overlap along the chord, effectively making a front and rear zone. The JFM grids were built in accordance to the best practices as established in the Drag Prediction Workshop.[4] When there is no support hardware included, two zones close off the rear end of the fuselage. When the support hardware is present, one zone models the fuselage-sting coupler. The sting is made up of two zones, one long periodic grid spanning the length of the sting, and an end cap. The mast is made up of 6 zones, three modeling the mast top, one for the mast bottom as it extends to the tunnel floor, and two connecting the mast to the sting. The JFM grids with no support hardware to all the support hardware ranged from 42 million to 46 million grid points.

The following cases were run using OVERFLOW: (1) Baseline 14x22 + JFM, (2) Baseline 14x22 + JFM + Sting, (3) Baseline 14x22 + JFM + Sting + Mast, (4) Inviscid Extended Diffuser 14x22 + JFM + Sting + Mast. A full angle of attack sweep was run, but we will only show results at α = 5.0 degrees for brevity. The same run conditions were utilized for all of the cases, namely M = 0.2, Re = 2.4 million based on crank chord, and the SA-RC-QCR2000 turbulence model.

4.2 Support Hardware Sensitivity at α=5.0°

Figure 11 shows the flowfield along the Y=0 slice for the various fidelities of support hardware. The support hardware does not seem to change the upstream flowfield. The Mach contour levels and shape are very similar from the start of the test section through the rear of the fuselage. The pressure coefficient contours for all of the configurations were nearly identical, and resemble Figure 12-4. Figure 12-1 to Figure 12-3 shows the pressure coefficient differences from each configuration to the solution in Figure 12-4 on the model, by taking each solution and subtracting the solution from Figure 12-4. The pressure coefficient differences are on the order of 0.02, and are mostly located at the leading edge horseshoe vortex and the wing tip. This small difference can probably be attributed to the small tunnel speed differences between each case. Figure 13 shows surface streamlines highlighting the side of body separation, and the differences are indistinguishable for all the configurations. The support hardware does not seem to significantly affect the solution computed on the wing.

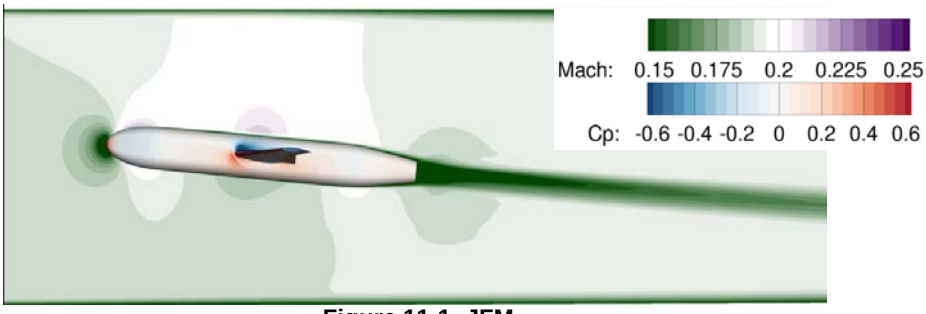

Figure 11-1: JFM

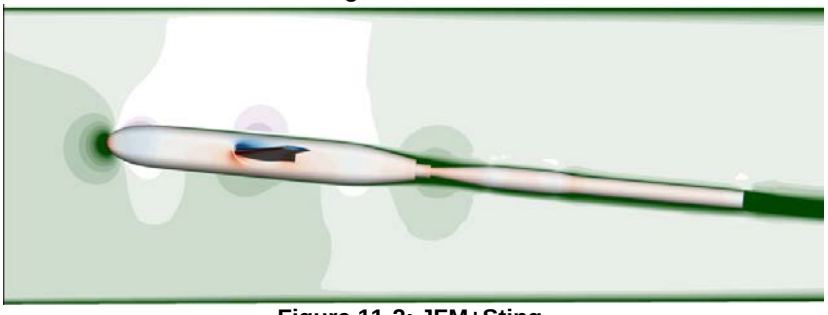

Figure 11-2: JFM+Sting

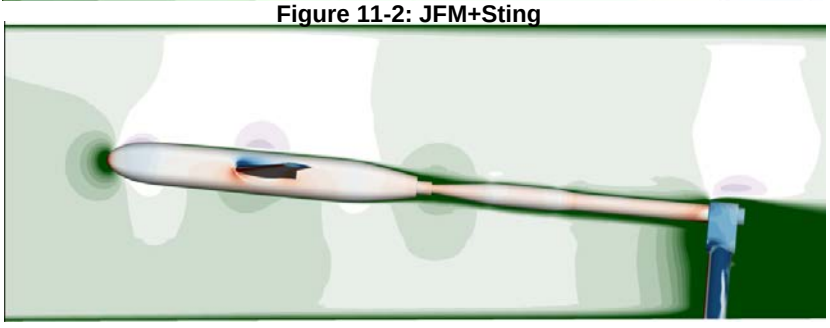

Figure 11-3: JFM+Sting+Mast

Figure 11: Y=0 Slice showing Mach contours, JFM colored by pressure contours, JFM support hardware study in 14x22 test section, α = 5°

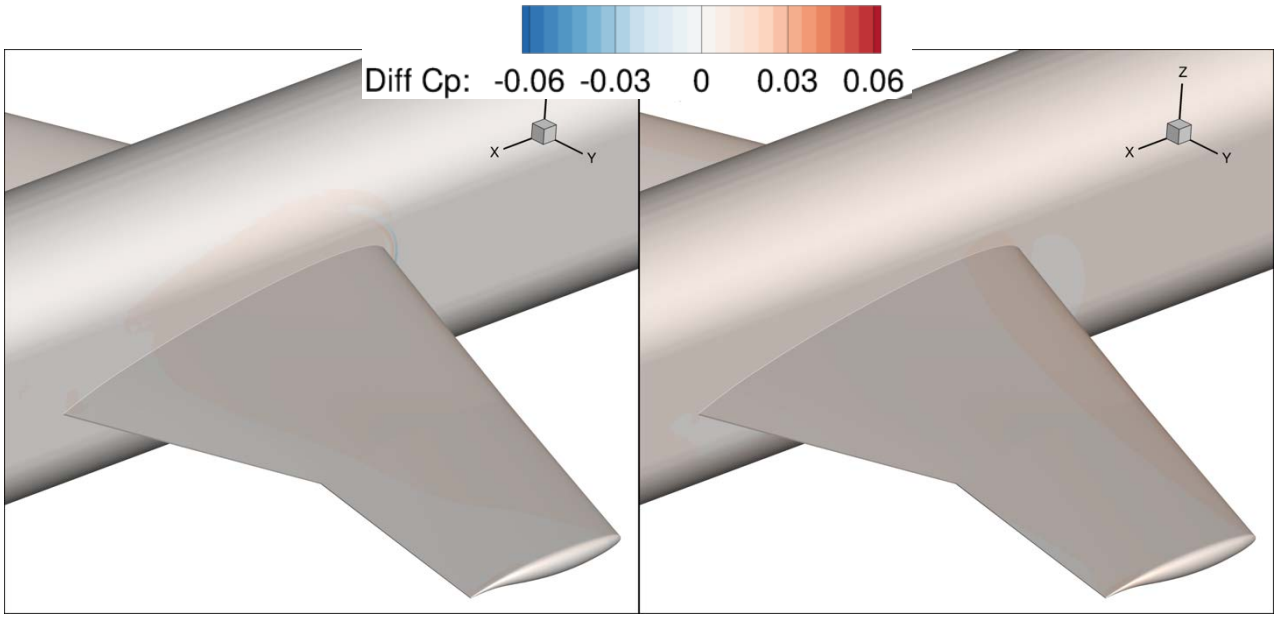

Figure 12-1: Baseline 14x22 JFM, ΔCp

Figure 12-2: Baseline 14x22 JFM+Sting, ΔCp

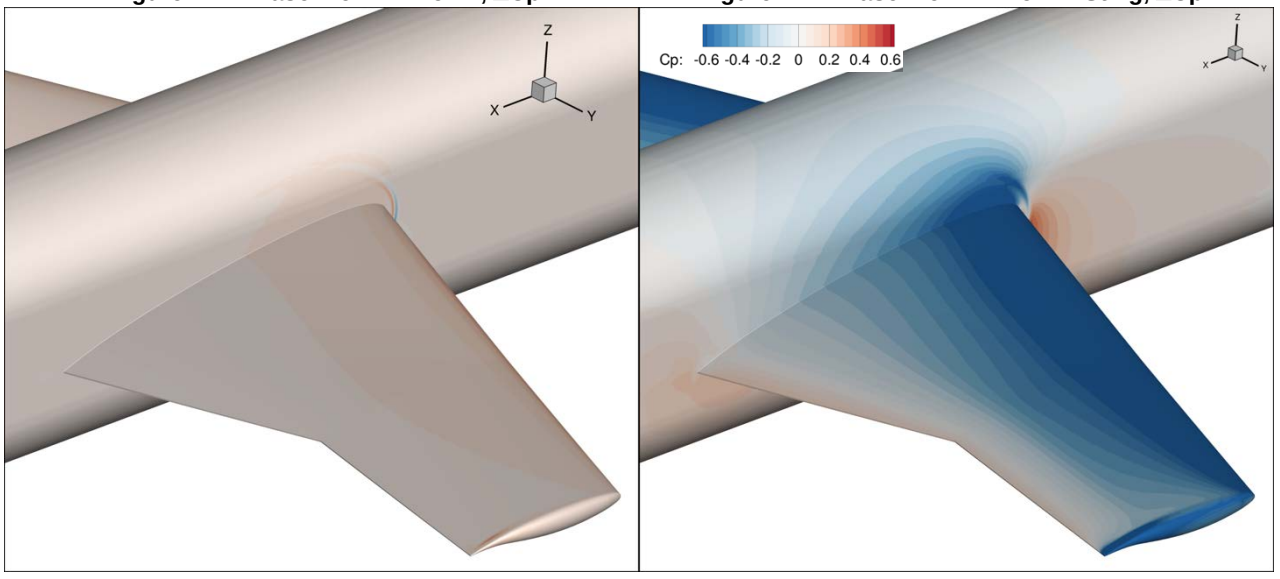

Figure 12-3: Baseline 14x22 JFM+Sting+Mast, ΔCp

Figure 12-4: Extended 14x22 JFM+Sting+Mast, Cp

Figure 12: Pressure Coefficient Difference to 14x22 Extended JFM+Sting+Mast Solution, JFM support hardware effect on wing, $\alpha = 5°$

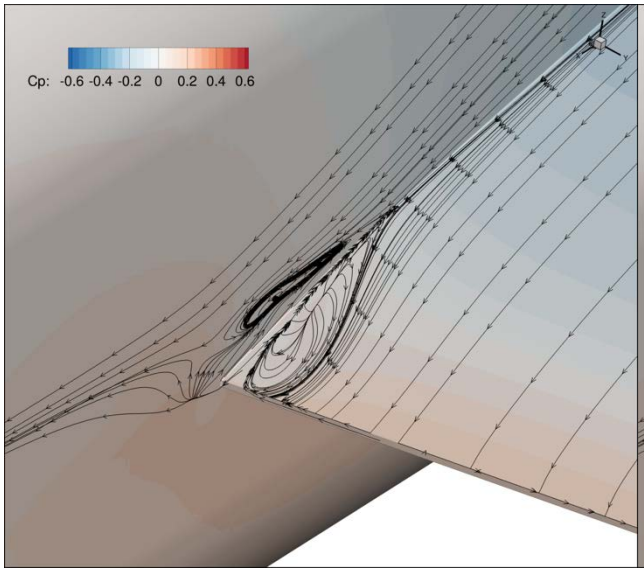

Figure 13-1: Baseline 14x22 JFM

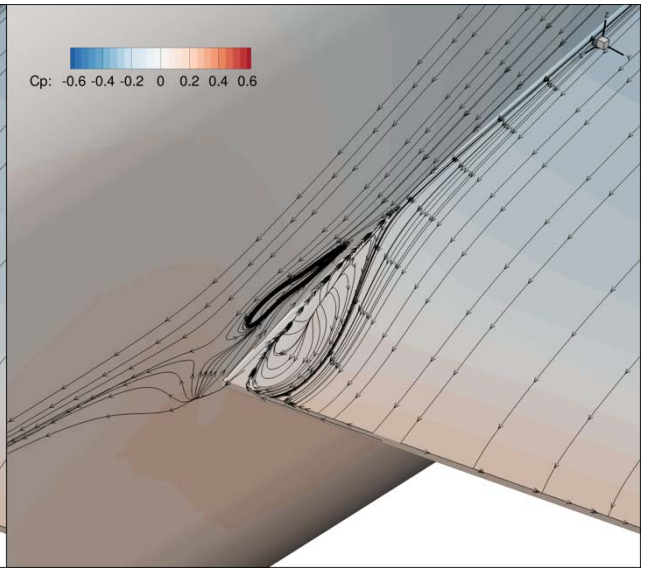

Figure 13-2: Baseline 14x22 JFM+Sting

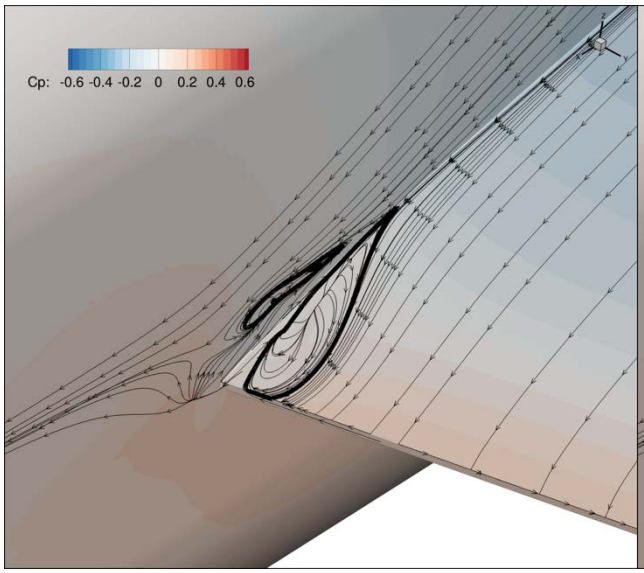

Figure 13-3: Baseline 14x22 JFM+Sting+Mast

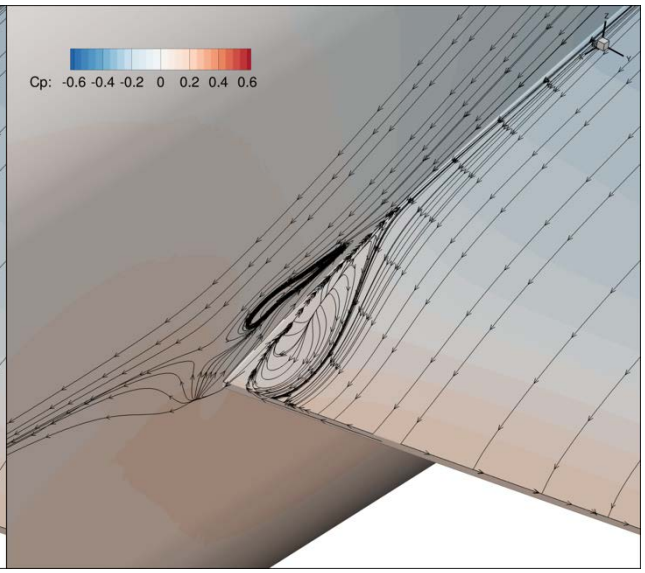

Figure 13-4: Extended 14x22 JFM+Sting+Mast

Figure 13: Surface Streamlines, JFM support hardware effect on wing side of body separation, α = 5°

4.3 Inviscid Extension Effect on JFM

Almost every JFM solution computed using the baseline tunnel grid system exhibited some sort of corner diffuser separation. Figure 14 shows the JFM solution inside the 14x22 at α=5.0 degrees, with various levels of support hardware modeled. The gray isosurfaces highlight corner separation. Only Figure 14-4, the simulation computed using the inviscid diffuser extension, did not exhibit large corner separation. Figure 15 shows the tunnel Mach number convergence, based on method 2 outlined in section 2.5.2 (using the static and stagnation pressure probes). Cases with corner separation, as shown in Figure 15-1 through Figure 15-3, computed a very noisy tunnel speed.

Small changes to the exit pressure ratio can trigger large oscillations, as seen in Figure 15-1 and Figure 15-2, in the tunnel speed computation. These large oscillations require a large number of iterations to dampen out, resulting in a larger computational cost. With the inviscid diffuser extension, the tunnel speed reaches an equilibrium in fewer steps, as seen in Figure 15-4. Figure 16 shows the resulting exit pressure ratio needed to achieve a tunnel speed of Mach 0.2, for all the cases and angles of attack. The exit pressure ratio is highly erratic at the higher angles of attack for the baseline grid (labeled WT), while the extended wind tunnel (labeled WTExt) exit pressure is fairly constant at all angles of attack. Higher blockage and wing loading may contribute to the corner separation in the diffuser.

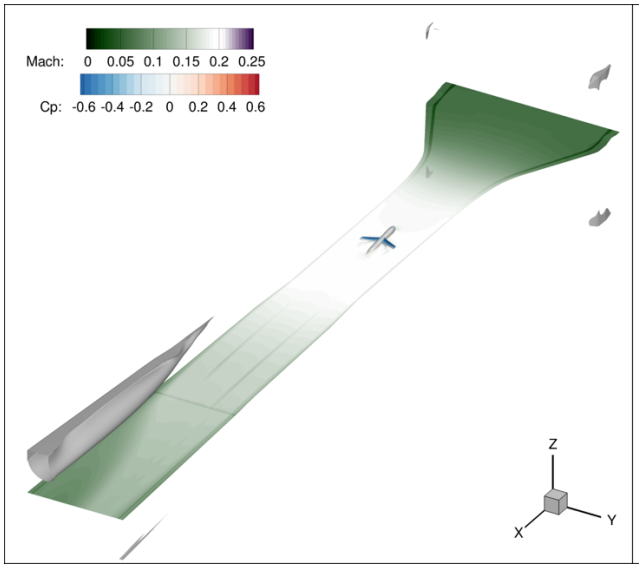

Figure 14-1: Baseline 14x22 JFM

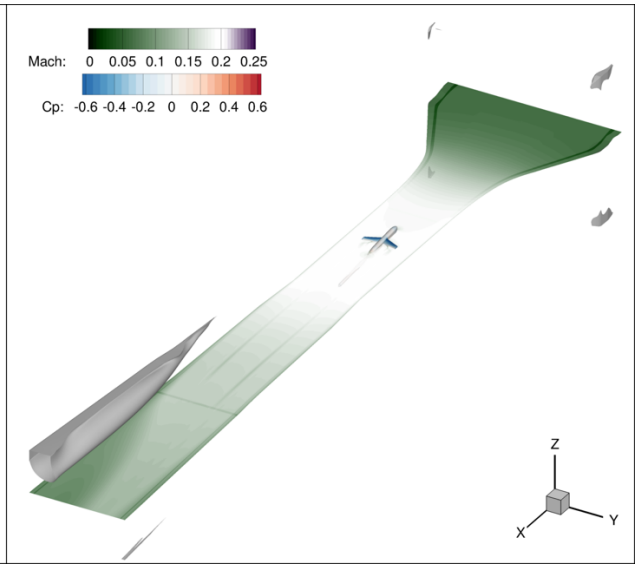

Figure 14-2: Baseline 14x22 JFM+Sting

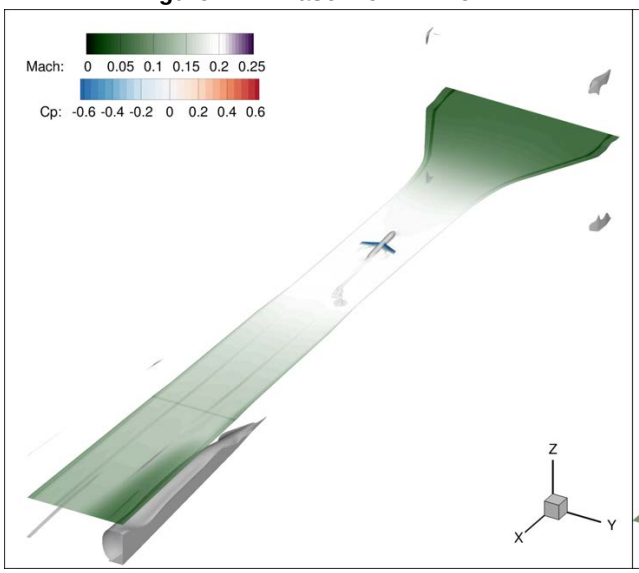

Figure 14-3: Baseline 14x22 JFM+Sting+Mast

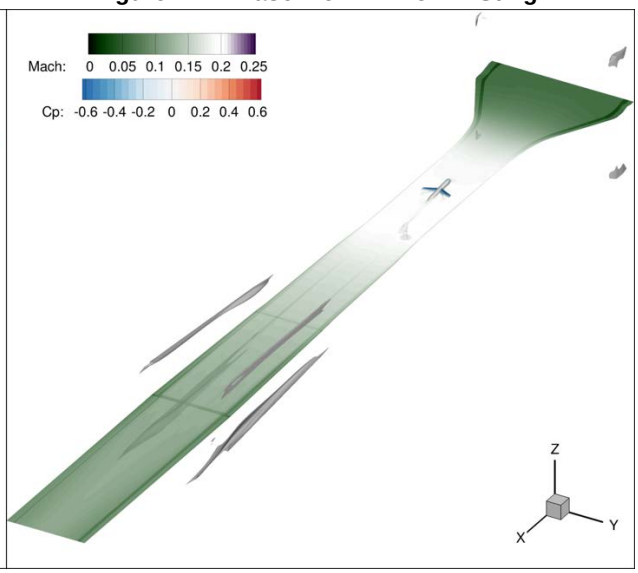

Figure 14-4: Extended 14x22 JFM+Sting+Mast

Figure 14: Y=0 Slice colored by Mach contours and gray isosurfaces representing reverse flow, Inviscid diffuser extension effect on JFM, α = 5°

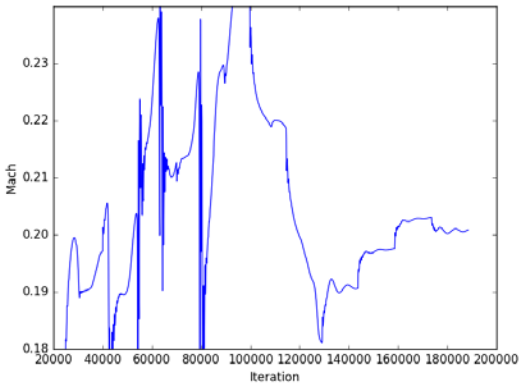

Figure 15-1: Baseline 14x22 JFM

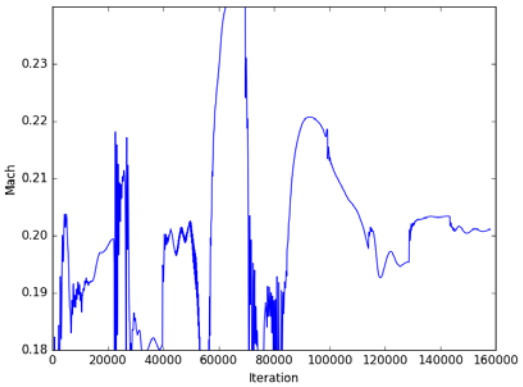

Figure 15-2: Baseline 14x22 JFM+Sting

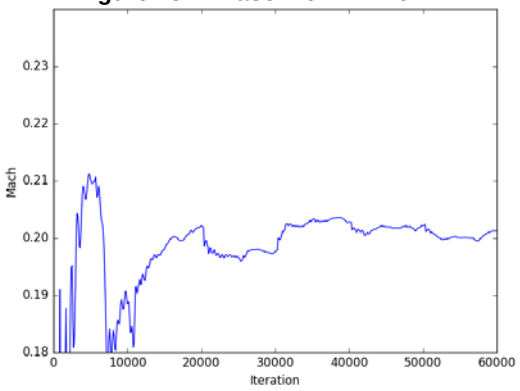

Figure 15-3: Baseline 14x22 JFM+Sting+Mast

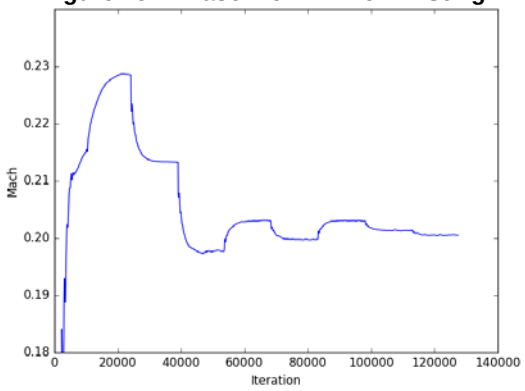

Figure 15-4: Extended 14x22 JFM+Sting+Mast

Figure 15: Tunnel speed convergence, Inviscid diffuser extension effect on JFM, α = 5.0°

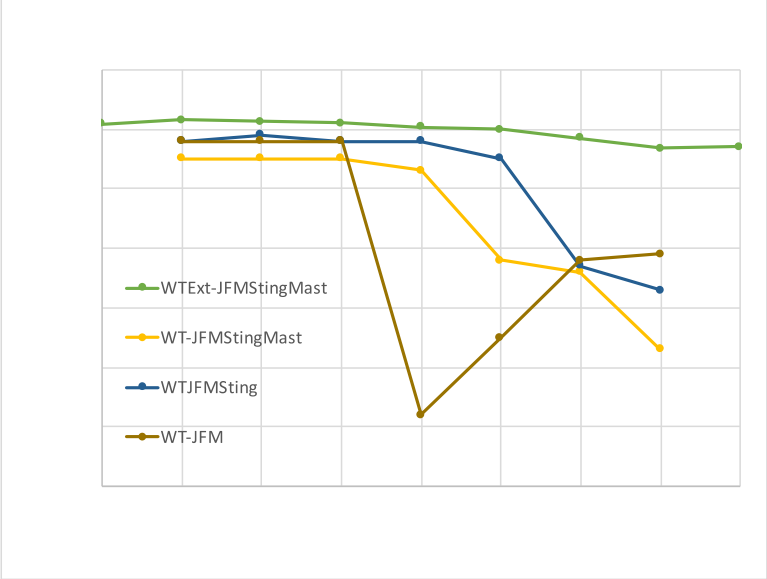

Figure 16: Exit Pressure Ratio, Inviscid diffuser extension vs baseline tunnel with various JFM support hardware

5.0 SUMMARY

This paper described a wide range of studies connected to the NASA Juncture Flow (JF) project, all with the common theme of determining and assessing modeling strategies for the JF model in the NASA Langley 14- by 22-Foot Subsonic Tunnel.

CFD viscous wall solutions with corner separation in the diffuser were problematic to converge, but strategies to overcome these issues, involving using an inviscid inlet and inviscid extended diffuser, seem promising. More in-depth CFD studies are needed to determine this corner separation sensitivity to CFD inputs.

With a model installed in the tunnel, setting the "correct" corresponding tunnel boundary conditions can be challenging for CFD. OVERFLOW made use of measured total and static pressures at specific upstream locations, and iterated on the back pressure. In the future, other measurements such as static pressures in the diffuser should help CFD.

Finally, some parametric CFD studies were conducted for the JFM to determine sensitivities of the flow near the wing-body juncture region of the model to the support hardware. A brief study in minimizing the corner separation was explored, but further study is needed. Very minimal effect of the hardware on the JF region of interest was found. A brief study in minimizing the diffuser corner separation was explored, but further study is needed. The wall effects and nonuniformities in the inflow boundary still need to be studied.

Ultimately, with highly detailed wind tunnel tests geared specifically for CFD validation, we would like to gather enough information so that CFD can unambiguously run "apples-to-apples" CFD to experiment comparisons. In this way, lack of agreement caused by possible geometric and boundary condition differences will be off the table, leaving only modeling issues as the source. Then presumably, efforts to validate or improve the CFD models will be an easier task.

6.0 ACKNOWLEDGMENTS

This work was supported by NASA's Transformational Tools and Technologies (TTT) project of the Transformative Aeronautics Concepts Program (TACP).

7.0 REFERENCES

[1] Rumsey, C. L., Carlson, J., Hannon, J., Jenkins L., Bartram, S., Pulliam, T., and Lee, H., "Boundary Condition Study for the Juncture Flow Experiment in the NASA Langley 14x22-Foot Subsonic Wind Tunnel," AIAA Paper 2017-4126, June 2017

[2] Kegerise, M. A. and Neuhart, D. H., "Wind Tunnel Test of a Risk-Reduction Wing/Fuselage Model to Examine Juncture-Flow Phenomena," NASA TM–219348, November 2016.

[3] Rumsey, C., Neuhart, D., and Kegerise, M., "The NASA Juncture Flow Experiment: Goals, Progress, and Preliminary Testing," AIAA Paper 2016–1557, January 2016.

[4] Vassberg, J., Tinoco, E., Mani, M., Brodersen, O., Eisfeld, B., Wahls, R., Morrison, J., Zickuhr, T., Laflin, K., and Mavriplis, D., "Abridged Summary of the Third AIAA Computational Fluid Dynamics Drag Prediction Workshop," AIAA Journal of Aircraft, Vol. 45, No. 3, 2008, pp. 781–798.

[5] Aeschliman, D. and Oberkampf, W., "Experimental Methodology for Computational Fluid Dynamics Code Validation," AIAA Journal, Vol. 36, No. 5, 1998, pp. 773–741.

[6] Nayani, S., Sellers, W., Brynildsen, S., and Everhart, J., "Numerical Study of the High-Speed Leg of a Wind Tunnel," AIAA Paper 2015–2022, January 2015.

[7] Nayani, S., Sellers, W., Tinetti, A., Brynildsen, S., and Walker, E., "Numerical Simulation of a Complete Low-Speed Wind Tunnel Circuit," AIAA Paper 2016–2117, January 2016.

[8] Roe, P. L., "Approximate Riemann Solvers, Parameter Vectors, and Difference Schemes," J. Comp. Phys., Vol. 43, 1981, pp. 357–372.

[9] Suhs, N. E., Rogers, S. E., and Dietz, W. E., "PEGASUS 5: An Automated Pre-processor for Overset-Grid CFD," AIAA Journal, Vol. 41, No. 6, 2003.

[10] Meakin, R. L., "Object X-Rays for Cutting Holes in Composite Overset Structured Grids," AIAA Paper 2001–2537, June 2001.

[11] https://overflow.larc.nasa.gov, Accessed: 2017-03-20.

[12] Spalart, P. R. and Allmaras, S. R., "A One-Equation Turbulence Model for Aerodynamic Flows," Recherche Aerospatiale, Vol. 1, 1994, pp. 5–21.

[13] Shur, M. L., Strelets, M. K., Travin, A. K., and Spalart, P. R., "Turbulence Modeling in Rotating and Curved Channels: Assessing the Spalart-Shur Correction," AIAA Journal, Vol. 38, No. 5, 2000, pp. 784–792.

[14] Spalart, P. R., "Strategies for Turbulence Modelling and Simulation," International Journal of Heat and Fluid Flow, Vol. 21, 2000, pp. 252–263.

[15] Carlson, J., "Inflow/Outflow Boundary Conditions with Application to FUN3D," NASA TM–2011-217181, October 2011.

[16] Jirasek, A., "Mass Flow Boundary Conditions for Subsonic Inflow and Outflow Boundary," AIAA Journal, Vol. 44, No. 5, 2006, pp. 939–947.

[17] Chung, J. and Cole, G., "Comparison of Compressor Face Boundary Conditions for Unsteady CFD Simulations of Supersonic Inlets," AIAA Paper 1995–2627, July 1995.

[18] Atkins, H. and Casper, J., "Nonreflective Boundary Conditions for High-Order Methods," AIAA Journal, Vol. 32, No. 3, 1994, pp. 512–518.

[19] Tam, C.-J., Eklund, D., and Behdadnia, R., "Influence of Downstream Boundary Conditions on Scramjet-Isolator Simulations," AIAA Paper 2008–6929, August 2008.

[20] Chan, W. M., Gomez, R. J., Rogers, S. E., and Buning, P. G., "Best Practices in Overset the Grid Generation," AIAA Paper 2002-3191, Jun. 2002.

[21] Gentry Jr, C. L., Quinto, P., Gatlin, G., and Applin, Z., "The Langley 14- by 22-Foot Subsonic Tunnel: Description, Flow Characteristics, and Guide for Users," NASA TP–3008, September 1990.

[22] Lee, H., Pulliam, T., Neuhart, D., and Kegerise, M., "CFD Analysis in Advance of the NASA Juncture Flow Experiment," AIAA Paper 2017-4127, June 2017

[23] http://turbmodels.larc.nasa.gov, Accessed: 2017-03-21.